# Dual-Frequency Peak Force Photothermal Microscopy for Simultaneously Spatial Mapping Chemical Distributions and Energy Dissipation

Qing Xie<sup>1</sup>, Haomin Wang<sup>2</sup>, and Xiaoji G Xu<sup>1\*</sup>

<sup>1</sup>Department of Chemistry, Lehigh University, 6 E Packer Ave. Bethlehem, PA, 18015, United States

<sup>2</sup>Division of Chemistry and Chemical Engineering, California Institute of Technology, 1200 E California Blvd, Pasadena, CA, 91125, United States

Email: xgx214@lehigh.edu

#### Abstract:

Deciphering correlations between physical properties at the nanoscale requires multimodal measurement with high spatial resolution at the nanometer scale. One platform to achieve multimodal imaging is through scanning probe microscopy. In this article, we report the development of dual-frequency peak force photothermal microscopy, which is a multimodal atomic force microscopy (AFM)-based spectroscopic imaging method. The method delivers simultaneous infrared and visible nanoscopy within one AFM scan frame, mapping the distribution of chemical components from infrared absorption and photothermal responses from electronic transitions. We apply this new method to organic-inorganic perovskite photovoltaics material, revealing chemical distributions at the surface and detecting localized heat generation. In addition, we observe that the photothermal heat generation appears at the back side of the light illumination direction due to local optical field distributions around nanoscale grains. As a measurement tool, dual-frequency peak force photothermal microscopy is expected to facilitate the characterizations of novel photovoltaic materials through correlative mapping of chemicals and optical absorption properties.

#### Introduction

Spectroscopic imaging at a spatial resolution below Abbe's diffraction limit has been challenging for traditional microscopy. Nanometer-scale feature cannot be straightforwardly resolved below the half wavelength of the photons, which is several hundreds of nanometers for visible light and several microns

for the infrared (IR). On the other hand, nanoscale heterogeneity is widely present in photovoltaic materials. For example, the behavior of the heterojunction organic photovoltaics is controlled by its nanoscale phase separation<sup>2</sup> and is linked with its surface morphology and conditions.<sup>3</sup> The perovskite film with the uniform surface condition often yields better performance.<sup>4</sup> Imaging methods, such as regular atomic force microscopy (AFM) and electron microscopy (EM), are suitable to measure the morphology of the sample with nanometer resolution; however, both AFM and EM are usually not spectroscopic. They provide little information on the nanoscale chemical distribution or how photovoltaics responds to light.

The advantage of spectroscopic imaging stems from the targeted choice of the excitation wavelength. The IR absorption reveals the chemical composition through characteristic IR-active functional groups of photovoltaic materials. The light-matter interaction with visible or ultraviolet (UV) light generates excitons, or charge carriers, initiating photophysical processes that are critical for solar energy conversion. Consequently, the combination of IR and UV-visible spectroscopies has become standard practice for the characterization of photovoltaic materials. However, due to spatial resolution limitations, the challenge of spectroscopic imaging at the nanoscale remains.

The combination of AFM and laser illumination provides feasible routes for label-free superresolution spectroscopic imaging of photovoltaic materials. One route is utilizing the near-field scattering by a metallic AFM tip. 6-14 The scattered light by the tip at the proximity of the sample probes electromagnetic fields with higher spatial frequencies than the propagating photons. Spectroscopic nanoimaging is achieved through scanning the position of the AFM tip and using interferometric detection of the near-field scattered light. However, the interferometric detection of scattering-type near-field microscopy requires high instrument complexity. In the case of operation with a short wavelength, high stability of the interferometer is required for maintaining imaging quality. Another popular route of AFMbased spectroscopy is through the mechanical detection of the photothermal response by the AFM tip. 15-17 The confined electromagnetic field created by the sharp metallic AFM tip under external light illumination can locally excite resonances in the sample with a matching light wavelength. The relaxation of the excited states after light-matter-interaction eventually leads to heat generation, which usually causes volume expansion of the sample. 18-19 The AFM tip mechanically detects such photothermal expansions. AFM-based photothermal microscopy has been increasingly popular. <sup>20</sup> The AFM photothermal microscopy with visible excitation has also been implemented to probe the electronic absorption of the sample. <sup>21-23</sup> However, there is not yet a platform of AFM-based photothermal microscopy with simultaneous measurement with IR and visible excitations, which would be instrumental for studying novel photovoltaic materials.

In this article, we seek to address the need for *in situ* measurements of photovoltaics with the integration of AFM-based IR and visible photothermal microscopy. We combine the methods of peak force

infrared (PFIR) microscopy<sup>24</sup> and peak force visible (PF-vis) microscopy<sup>21</sup> into one measurement apparatus, simultaneously delivering chemical mapping and optical property measurement. With this new tool, we studied the organic-inorganic halide perovskite film of Cs<sub>0.05</sub>(FA<sub>0.93</sub>MA<sub>0.07</sub>)<sub>0.95</sub>PbI<sub>3</sub>, identifying the local compositional heterogeneity through nanoscale IR imaging. In addition, we have also observed a counterintuitive phenomenon: the localized heat generation situates within sample grains at the back side from the visible light illumination. We interpret this observation as a result of photodoping and the long diffusion range of charge carriers.

# Method and operational principle

The method that we developed for this research is through integrating the PFIR microscopy and the PF-visible microscopy. Both PFIR and PF-visible microscopies were developed in our group earlier and described in the literature.<sup>21, 24</sup> The essence of these two methods is the mechanical detection of the photothermal responses of the sample with an AFM, operated in the peak force tapping mode or pulsed force mode.<sup>25-26</sup> The sample absorbs the infrared or visible radiations according to its vibrational and electronic resonances. The infrared absorption from vibrational resonances is characteristic of functional groups and chemical composition; the electronic resonances are typically within the visible frequency range for photovoltaics. The subsequent relaxations of the excited states release heat and usually cause the sample to expand according to the temperature increase. Such photothermal expansions are detected by the deflections and oscillations of the AFM probe.<sup>15-16</sup> Through analyzing the mechanical responses from the AFM cantilever, the magnitude of the infrared or visible absorption can be extracted. In our experimental implementation, we adopted the simultaneous detection configuration of the dual-color PFIR microscopy<sup>27</sup> to incorporate both the infrared excitation and the visible excitations. The AFM-based photothermal imaging of both infrared and visible frequencies is done simultaneously in one AFM frame scan.

As shown in Figure 1, an AFM (Multimode 8, Bruker) was operated under the peak force tapping (PFT) mode at 4 kHz frequency in the experimental implementation.<sup>25</sup> The AFM tip was periodically in contact with the sample surface at the PFT frequency with an externally controllable indentation force. A lock-in amplifier (MFLi, Zurich Instruments), acting as a phase-lock loop, was used to generate two replicas of the phase-synchronized transistor to transistor logic (TTL) waveforms at half of the PFT frequency. There was a  $\pi$  phase offset between these two TTL waveforms. Each TTL waveform was routed as an external trigger to different laser sources: a quantum cascade laser (MIRcat-QT, Daylight Solutions) for emitting frequency tunable infrared pulses and a Q-switched visible laser at the wavelength of 532 nm (AO-S-532, CNI laser). The output of the visible laser was attenuated with an ND2 filter. The timing of the laser

emissions was controlled by adjusting the phase offset of the phase-lock loop so that the laser emissions were synchronized to moments when the AFM tip was in dynamic contact with the sample in the PFT mode. A long-wave pass filter combined the laser radiations from both lasers and expanded with a reflective telescope. The combined laser beams were then focused at the tip-sample region of the AFM with a parabolic mirror (f = 25 mm) at a 10-degree angle from the sample surface. The metal-coated AFM tip (HQ:NSC14/Pt, MikroMasch) amplified and localized the laser field underneath its apex and enhanced the light absorption. The heat generated from the light absorption caused photothermal expansions at a short time scale, which exerted a short duration force to the AFM tip to cause the deflections and subsequent cantilever oscillations. The cantilever deflection signal of the AFM was acquired by its built-in quadrant photodiode from a laser beam bounced off the back of the cantilever. The deflection signal was digitalized by an externally- triggered data acquisition card (PXI-5122, National Instruments) and processed in real-time by a customized Labview program on an embedded controller (PXIe-8135 National Instruments). The amplitudes of the cantilever oscillations due to the photothermal responses between the light-matter interactions were extracted through Fourier transform and recorded as the AFM tip was scanned over the sample surface at a scan rate of 0.15 Hz (256×256 pixels).

The photothermal signals from the IR absorption and the visible absorption were processed in parallel and simultaneously recorded in two channels. Because the laser emission for each light source was synchronized to half of the PFT frequency and interleaved in time, the infrared and visible photothermal responses were collected from consecutive PFT cycles without cross talks from the other signal channel. On the other hand, the time difference in two consecutive PFT cycles is about 250 µs, which is very small, compared with the scan time for one AFM frame, i.e., ~30 minutes. The infrared and the visible photothermal signals can be treated as being generated at the same sample location at almost the same time. This advantage allows for signal correlation analysis from each pixel from images of different signal channels without compromising frame drifts between different AFM modalities in consecutive AFM scans.

## Results

We studied the deposited film of the organic-inorganic perovskite Cs<sub>0.05</sub>(FA<sub>0.93</sub>MA<sub>0.07</sub>)<sub>0.95</sub>PbI<sub>3</sub> on an indium tin oxide (ITO) substrate with our dual-frequency peak force photothermal microscopy. The sample was obtained from a collaborator. The preparation procedure was described as one of the reference samples in the literature.<sup>4</sup> The crystal structure is plotted in Figure 2a. Figure 2b displays the topography of an area of the perovskite film. Figure 2c shows the infrared photothermal image collected from the PFIR channel of the apparatus. The IR excitation frequency is 1710 cm<sup>-1</sup>, which corresponds to the antisymmetric

C–N stretch of the FA component.<sup>28</sup> Figure 2d shows the PFIR image collected at 1589 cm<sup>-1</sup>, corresponding to the IR absorption from the antisymmetric bending of NH<sub>3</sub><sup>+</sup> in the MA component.<sup>28-29</sup> Figure 2e displays the PF-visible photothermal image with the 532 nm excitation wavelength. Figure 2b, 2c, and 2e were simultaneously collected in one AFM scan frame, and Figure 2d was collected in a subsequent AFM scan frame. Both the topography image (Figure 2b) and the PFIR image at 1710 cm<sup>-1</sup> (Figure 2c) suggest the surface of the perovskite film is not uniform, exhibiting nanoscale grains.

The patterns of the PFIR image at 1589 cm<sup>-1</sup> of MA functional groups (Figure 2d) follow the same overall distribution of the FA functional group as in Figure 2c, with reduced signal strength. This observation is consistent with the composition of the Cs<sub>0.05</sub>(FA<sub>0.93</sub>MA<sub>0.07</sub>)<sub>0.95</sub>PbI<sub>3</sub>, where the small concentration of the MA component is miscible with the main FA component without phase separation. On the other hand, an intriguing observation is a drastic difference in the spatial pattern of the PF-visible image of Figure 2e from that of the IR image of Figure 2c and 2d. The patterns of the PF-visible image exhibit a sharp boundary and show a certain level of alignment about 20 degrees to the horizontal axis of the image (Figure 2e).

What caused such an unusual distribution of the visible photothermal responses of this perovskite film? Was it due to the uneven chemical distribution? We collected the PFIR spectrum on two locations, 1 and 2, marked in Figure 2e. Location 1 has a low visible photothermal response, and location 2 has a high visible photothermal response. Their corresponding PFIR spectra from 1500 cm<sup>-1</sup> to 1758 cm<sup>-1</sup> are displayed in Figure 2f. The characteristic IR absorption of the FA component at 1710 cm<sup>-1</sup> is observed in both spectra. Despite a clear difference in the visible photothermal response, these two locations have almost identical IR absorption spectra---a lack of evidence in a significant difference of chemical compositions. Thus, the drastic difference in the photothermal responses in Figure 2e is not a result of heterogeneous chemical distribution.

We then performed the pixel-to-pixel (65536) correlative analysis between the PFIR signal at 1710 cm<sup>-1</sup> (Figure 2c) and the PF-visible signal at 532 nm (Figure 2e) as the correlation heat map (bivariate histogram plot, bin size = 100, generated with MATLAB). It is displayed in Figure 3, which shows two clusters. A dominant cluster to the left of the correlation map has a distribution of the IR photothermal response with low visible photothermal responses. The cluster corresponds to the regions of low PF-visible response in Figure 2e. The vertical orientation of this cluster shows a lack of correlation between the visible and the IR photothermal responses for the low PF-visible response region. In addition to the major cluster, a minor cluster exists (marked by the white dashed line) that exhibits a positive correlation between the IR photothermal response and the visible photothermal response at the higher signal range. This minor cluster corresponds to bright regions in Figure 2e. Such a positive correlation indicates that a high visible

photothermal response region corresponds to high IR responses. One of the factors that lead to high visible photothermal responses is also present for high IR response (but not *vice versa*), demonstrating the photothermal response is still from the FA-containing component, i.e., perovskite, and not the degradation product, i.e., PbI<sub>2</sub>.

How do we understand the origin of the localized PF-visible responses? Here, we closely examine our data using 3D rendering plots based on the sample topography. Figure 4a displays the 3D rendering of the topography of the sample. This 3D plot visualizes the sizes and locations of the perovskite grains. Figure 4b is the 3D rendering of the PF-visible signal overlaid on the sample topography. A green arrow indicates the illumination direction of the 532 nm laser. Figure 4c is the 3D rendering of the PFIR signal at 1710 cm $^{-1}$  overlaid on the sample topography. An intriguing feature is revealed by Figure 4b. The PF-visible signals appear behind the high areas of the sample away from the light illumination direction. In comparison, the PFIR signals lack such asymmetric features. The boundaries of the localized PF-visible signal also correlate with the nanoscale grains of the perovskite film. Because our laser illumination has only an angle of  $\sim 10$  degrees from the sample surface, regions of high roughness can have back sides behind the light illumination. The observed features suggest that the visible photothermal responses are localized with individual grains at the opposite side of the sample from the visible illumination. This observation is counterintuitive in a classic sense, as one would expect the side toward the light to be better illuminated, thus generating more photothermal effect that the back side.

## **Discussions**

How do we decipher the cause of such a counterintuitive observation on the location of photothermal generation with visible radiation? In our case, the measurement was done with the mechanical response of the AFM cantilever. Does the presence of the metallic AFM tip cause the non-uniform distribution of the photothermal effect? More specifically, does the metallic AFM tip enhances strongly the optical field when it is present at the grains at the backside of illumination? To answer these questions, we resort to finite element simulation method (Lumerical). Figure 5a displays the schematic configuration of the simulation. Two sphere represents two grains of perovskite of 200 nm radius of curvature. The light illumination angle was set at 10 degrees from the surface plane. The metallic tip was placed in three scenarios: at the front side of the grain towards the light illumination (marked by the dashed box 1); at the valley between two grains (marked by the dashed box 2); and at the backside of the grain away from the light illumination (marked by the dashed box 3). The distribution of the intensity of the electrical fields from these three scenarios are displayed in Figure 5b-d. In all cases, strong field enhancement is observed

between the tip and the sample grains. Although the electric field strength is slightly stronger when the tip is at the backside from the illumination, the maximal field strengths are comparable in all three cases. Tip enhancement dominates the field strength. If the photothermal responses in our measurement are only generated at the sample locations underneath the end sphere of the AFM tip, then the photothermal responses should follow the field enhancement. Thus, the photothermal response should not exhibit significant differences, as the maximal field strengths at the front side and back side are comparable in their intensity. However, the experimental observation of Figure 4 clearly shows a significant difference between the front side and back side of the illumination. This finding suggests that the photothermal response does not only originate from the area underneath the AFM tip.

We use the numerical simulation tool to further understand our observations. Figure 6a displays a simulation configuration of grains only, without the presence of the AFM tip. The light illumination direction was the same as Figure 5a, from the left side with 10 degrees. The intensity of the electric fields are shown in Figure 6b-d from three regions marked by the dashed boxes. The simulation of electrical field distribution shows that the back side of the nanoscale grain from the light illumination actually as a much stronger field strength than the front side of the grain. The plots of the simulation show that the field at back side (Figure 6d) from the light illumination is about ten times stronger than the front side (Figure 6b). The valley between two grains also supports an enhancement of the electric field. This is a unique nanooptical phenomenon for the nanoscale grains smaller than the wavelength of the light. Due to the wave nature of the light, the backside of a nanoscale grain experience stronger optical field than its frontside, under a small grazing angle. Thus, the carriers are more effectively generated in the grain at the back side of the light illumination. Although light-generated carriers has very long diffusion range,<sup>30</sup> they are more likely to be confined by the grain boundary. After the relaxation, the excited carriers recombine and generate heat to cause the whole grain to photothermally expand, leading to mechanical signals. As a result, the grains at the backside of the illumination exhibit stronger photothermal signals. The discontinuity of the photothermal signal follow the boundaries between grains. This interpretation agrees with the PF-visible measurement.

An interesting aspect of the simulations is that the maximal field intensity from the gap between the metallic tip and perovskite sample (as in Figure 5) is at least two orders of magnitude higher than the maximal field strength in absence of the AFM tip (as in Figure 6). On the other hand, the distribution of the photothermal response agrees with the field distribution *without* the presence of the AFM tip. How do we understand such a discrepancy? The distribution of the PF-visible response indicates that the ultrahigh field strength by the tip enhancement may have already entered the regime of strong absorption and stimulated emission. Due to high light absorption coefficient of perovskite and strong field enhancement by the

metallic tip, the population of the ground electronic state quickly approaches 1/2 of the total population by time average, and the absorption of photons of ground state are balanced by stimulated emission of photons. In a quantum interpretation, Rabi oscillation of the electronic transition of the perovskite possibly exists under the strong field enhancement by the AFM tip. The net result is the high field intensity does not translate into high overall optical absorption and energy dissipation. Thus, the distribution of the photothermal response deviate from the tip-enhancement. In contrast, the area outside the AFM tip is far from absorption saturation, and a bit higher field strength translates into more optical absorptions and heat generation. This interpretation is a possible explanation, given that the organic-inorganic perovskite has an excellent light absorption coefficient within the visible wavelength range<sup>31-32</sup> strong field enhancement by the tip, and nanosecond duration of our visible excitation laser.

From a method development perspective, our peak force dual-frequency photothermal microscopy has an advantage for correlative analysis of two simultaneously collected channels. There is no drift between the IR and the visible photothermal images. Two images from sequential measurements would always be associated with different frame distortions due to the piezo's hysteresis and thermal drift, which makes the pixel-to-pixel correlative analysis very difficult, if possible at all. On the other hand, our simultaneously collected images in one AFM scan always yield precise pixel-to-pixel correlation, making the analyzing correlation between measurement modalities possible.

Future applications of this method shall include the *in situ* measurement of the closed-circuit perovskite photovoltaic device.<sup>33</sup> When the photovoltaics function in a closed electrical circuit, charge separation occurs, and the heat generation should be somewhat suppressed, compared with the open-circuit measurement of only the perovskite film. A change in the spatial distribution in the PF-visible responses between the opened-circuit and closed-circuit conditions is expected, as the carrier is more likely to migrate across grain boundaries toward electrodes, instead of relaxation within grains. Furthermore, if an external bias voltage is applied, one may control the locations of energy loss through depleting or accumulating certain type of carrier to provide indications to the spatial distribution of carrier relaxation.

#### **Conclusions**

We have developed a tool for chemical measurement and imaging—the dual-frequency peak force photothermal microscopy for *in situ* visible and IR imaging, and demonstrated this technique on a perovskite film to map the chemical distribution and the energy dissipations. Based on the results from both the experiment and simulations, we observed that the distribution of the PF-visible response does not strictly correlate with the distribution of light-absorbing materials. Instead, it is located within perovskite grains at

the back side from the visible illumination, due to nanoscale optical field distributions. From a metrology method perspective, our dual-frequency peak force photothermal microscope collects both the visible and IR signals simultaneously, avoiding the frame drift and distortion from the consecutive scans. As an outlook, this technique should be used for characterizing closed-circuit perovskite photovoltaic devices and facilitating the future development of photovoltaics towards a carbon-neutral future.

# Acknowledgment

We want to thank Prof. Huanping Zhou and Dr. Nengxu Li for providing the perovskite sample. We would like to thank Ms. Andrea Dorsa for editing the manuscript. X. G. X. would like to thank the support from Beckman Young Investigator Award from the Arnold and Mabel Beckman Foundation, the Sloan Research Fellowship from the Alfred P. Sloan Foundation, and the Camille Dreyfus Teacher-Scholar Award from the Camille and Henry Dreyfus Foundation. Q.X. and X. G. X. would also like to thank the support from the National Science Foundation, award number CHE 1847765.

#### **References:**

- 1. Abbe, E., Beiträge zur Theorie des Mikroskops und der mikroskopischen Wahrnehmung. *Archiv Mikroskopische Anatomie* **1873**, *9* (1), 413-468.
- 2. Lee, H.; Park, C.; Sin, D. H.; Park, J. H.; Cho, K., Recent advances in morphology optimization for organic photovoltaics. *Adv. Mater.* **2018**, *30* (34), 1800453.
- 3. Salim, T.; Sun, S.; Abe, Y.; Krishna, A.; Grimsdale, A. C.; Lam, Y. M., Perovskite-based solar cells: impact of morphology and device architecture on device performance. *J. Mater. Chem. A* **2015**, *3* (17), 8943-8969.
- 4. Li, N., Niu, X., Li, L., Wang, H., Huang, Z., Zhang, Y., Chen, Y., Zhang, X., Zhu, C. Zai, H., et al., Liquid medium annealing for fabricating durable perovskite solar cells with improved reproducibility. *Science* **2021**, *373* (6554), 561-567.
- 5. Terazima, M., Hirota, N., Braslavsky, S. E., Mandelis, A., Bialkowski, S. E., Diebold, G. J., Miller, R., Fournier, D., Palmer, R. A. and Tam, A., Quantities, terminology, and symbols in photothermal and related spectroscopies (IUPAC Recommendations 2004). *Pure Appl. Chem.* **2004**, *76* (6), 1083-1118.
- 6. Inouye, Y.; Kawata, S., Near-field scanning optical microscope with a metallic probe tip. *Opt. Lett.* **1994,** *19* (3), 159-161.
- 7. Bachelot, R.; Gleyzes, P.; Boccara, A., Near-field optical microscope based on local perturbation of a diffraction spot. *Opt. Lett.* **1995**, *20* (18), 1924-1926.
- 8. Lahrech, A.; Bachelot, R.; Gleyzes, P.; Boccara, A., Infrared-reflection-mode near-field microscopy using an apertureless probe with a resolution of  $\lambda/600$ . *Opt. Lett.* **1996,** 21 (17), 1315-1317.
- 9. Bachelot, R.; Gleyzes, P.; Boccara, A., Reflection-mode scanning near-field optical microscopy using an apertureless metallic tip. *Appl. Opt.* **1997**, *36* (10), 2160-2170.
- 10. Knoll, B.; Keilmann, F., Near-field probing of vibrational absorption for chemical microscopy. *Nature* **1999**, *399* (6732), 134-137.
- 11. Keilmann, F.; Hillenbrand, R., Near-field microscopy by elastic light scattering from a tip. *Phil. Trans. R. Soc. A.* **2004**, *362* (1817), 787-805.
- 12. Ichimura, T.; Fujii, S.; Verma, P.; Yano, T.; Inouye, Y.; Kawata, S., Subnanometric near-field Raman investigation in the vicinity of a metallic nanostructure. *Phys. Rev. Lett.* **2009**, *102* (18), 186101.
- 13. Wang, L.; Xu, X. G., Scattering-type scanning near-field optical microscopy with reconstruction of vertical interaction. *Nat. Commun.* **2015**, *6* (1), 1-9.
- 14. Chen, X.; Hu, D.; Mescall, R.; You, G.; Basov, D. N.; Dai, Q.; Liu, M., Modern scattering-type scanning near-field optical microscopy for advanced material research. *Adv. Mater.* **2019**, *31* (24), 1804774.
- 15. Anderson, M. S., Infrared spectroscopy with an atomic force microscope. *Appl. Spectrosc.* **2000**, *54* (3), 349-352.
- 16. Dazzi, A.; Prazeres, R.; Glotin, F.; Ortega, J. M., Local infrared microspectroscopy with subwavelength spatial resolution with an atomic force microscope tip used as a photothermal sensor. *Opt. Lett.* **2005**, *30* (18), 2388-2390.
- 17. Nowak, D.; Morrison, W.; Wickramasinghe, H. K.; Jahng, J.; Potma, E.; Wan, L.; Ruiz, R.; Albrecht Thomas, R.; Schmidt, K.; Frommer, J., et al., Nanoscale chemical imaging by photoinduced force microscopy. *Sci. Adv.* 2 (3), e1501571.
- 18. Li, Z.; Aleshire, K.; Kuno, M.; Hartland, G. V., Super-Resolution Far-Field Infrared Imaging by Photothermal Heterodyne Imaging. *J. Phys. Chem. B* **2017**, *121* (37), 8838-8846.
- 19. Zhang, D.; Li, C.; Zhang, C.; Slipchenko, M. N.; Eakins, G.; Cheng, J.-X., Depth-resolved mid-infrared photothermal imaging of living cells and organisms with submicrometer spatial resolution. *Sci. Adv.* **2016**, *2* (9), e1600521.
- 20. Kurouski, D.; Dazzi, A.; Zenobi, R.; Centrone, A., Infrared and Raman chemical imaging and spectroscopy at the nanoscale. *Chem. Soc. Rev.* **2020**, *49* (11), 3315-3347.

- 21. Wang, H.; Wang, L.; Shang, Y.; Tafti, S. Y.; Cao, W.; Ning, Z.; Zhang, X. F.; Xu, X. G., Peak force visible microscopy. *Soft Matter* **2020**, *16* (36), 8372-8379.
- 22. Katzenmeyer, A. M.; Holland, G.; Kjoller, K.; Centrone, A., Absorption Spectroscopy and Imaging from the Visible through Mid-Infrared with 20 nm Resolution. *Anal. Chem.* **2015**, 87 (6), 3154-3159.
- 23. Strelcov, E.; Dong, Q.; Li, T.; Chae, J.; Shao, Y.; Deng, Y.; Gruverman, A.; Huang, J.; Centrone, A., CH<sub>3</sub>NH<sub>3</sub>PbI<sub>3</sub> perovskites: Ferroelasticity revealed. *Sci. Adv.* **2017**, *3* (4), e1602165.
- 24. Wang, L.; Wang, H.; Wagner, M.; Yan, Y.; Jakob, D. S.; Xu, X. G., Nanoscale simultaneous chemical and mechanical imaging via peak force infrared microscopy. *Sci. Adv.* **2017**, *3* (6), e1700255.
- 25. Pittenger, B.; Erina, N.; Su, C., Quantitative mechanical property mapping at the nanoscale with PeakForce QNM. *Bruker Application Note*, **2010**, *ANI28*, *Rev. A*.
- 26. Rosa-Zeiser, A.; Weilandt, E.; Hild, S.; Marti, O., The simultaneous measurement of elastic, electrostatic and adhesive properties by scanning force microscopy: pulsed-force mode operation. *Meas. Sci. Technol.* **1997**, *8* (11), 1333-1338.
- 27. Xie, Q.; Wiemann, J.; Yu, Y.; Xu, X. G., Dual-Color Peak Force Infrared Microscopy. *Anal. Chem.* **2022**, *94* (2), 1425-1431.
- 28. Szostak, R.; Silva, J.; Turren-Cruz, S.-H.; Soares, M.; Freitas, R.; Hagfeldt, A.; Tolentino, H.; Nogueira, A., Nanoscale mapping of chemical composition in organic-inorganic hybrid perovskite films. *Sci. Adv.* **2019**, *5* (10), eaaw6619.
- 29. Glaser, T.; Müller, C.; Sendner, M.; Krekeler, C.; Semonin, O. E.; Hull, T. D.; Yaffe, O.; Owen, J. S.; Kowalsky, W.; Pucci, A., et al., Infrared Spectroscopic Study of Vibrational Modes in Methylammonium Lead Halide Perovskites. *J. Phys. Chem. Lett.* **2015**, *6* (15), 2913-2918.
- 30. Guo, Z.; Wan, Y.; Yang, M.; Snaider, J.; Zhu, K.; Huang, L., Long-range hot-carrier transport in hybrid perovskites visualized by ultrafast microscopy. *Science* **2017**, *356* (6333), 59-62.
- 31. El-Ghtami, H.; Laref, A.; Laref, S., Electronic and optical behaviors of methylammonium and formamidinium lead trihalide perovskite materials. *J. Mater. Sci.: Mater. Electron.* **2019**, *30* (1), 711-720.
- 32. Kato, M.; Fujiseki, T.; Miyadera, T.; Sugita, T.; Fujimoto, S.; Tamakoshi, M.; Chikamatsu, M.; Fujiwara, H., Universal rules for visible-light absorption in hybrid perovskite materials. *J. Appl. Phys.* **2017**, *121* (11), 115501.
- 33. Singh, G. K., Solar power generation by PV (photovoltaic) technology: A review. *Energy* **2013**, *53*, 1-13.

# Figures:

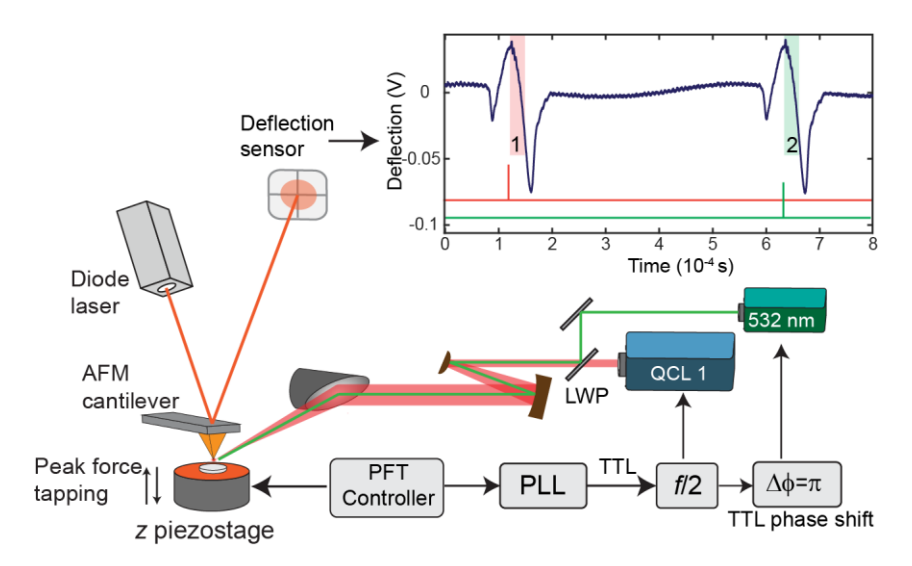
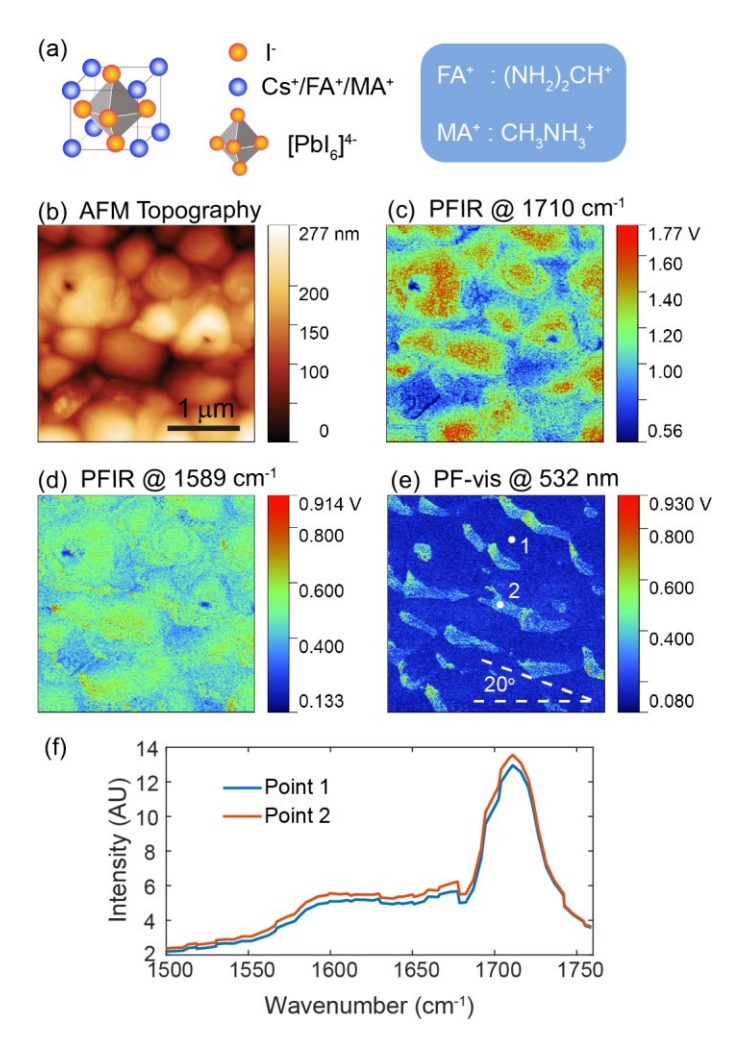
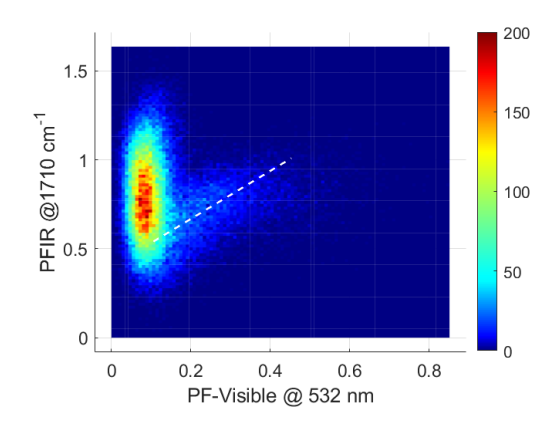


Figure 1. The experimental setup of a dual-frequency peak force photothermal microscopy.



**Figure 2.** Dual-frequency peak force photothermal microscopy on perovskite film. (a) Crystal structure of the perovskite sample. (b) AFM topography. (c) PFIR image at 1710 cm<sup>-1</sup>, which is in resonant with the PA component. (d) PFIR image at 1589 cm<sup>-1</sup> is resonant with the MA component. (e) PF-visible image at 532 nm excitation wavelength. (f) PFIR spectra from two locations marked as 1 and 2 in panel 2e.



**Figure 3.** Correlative map between the PFIR and PF-visible signal.

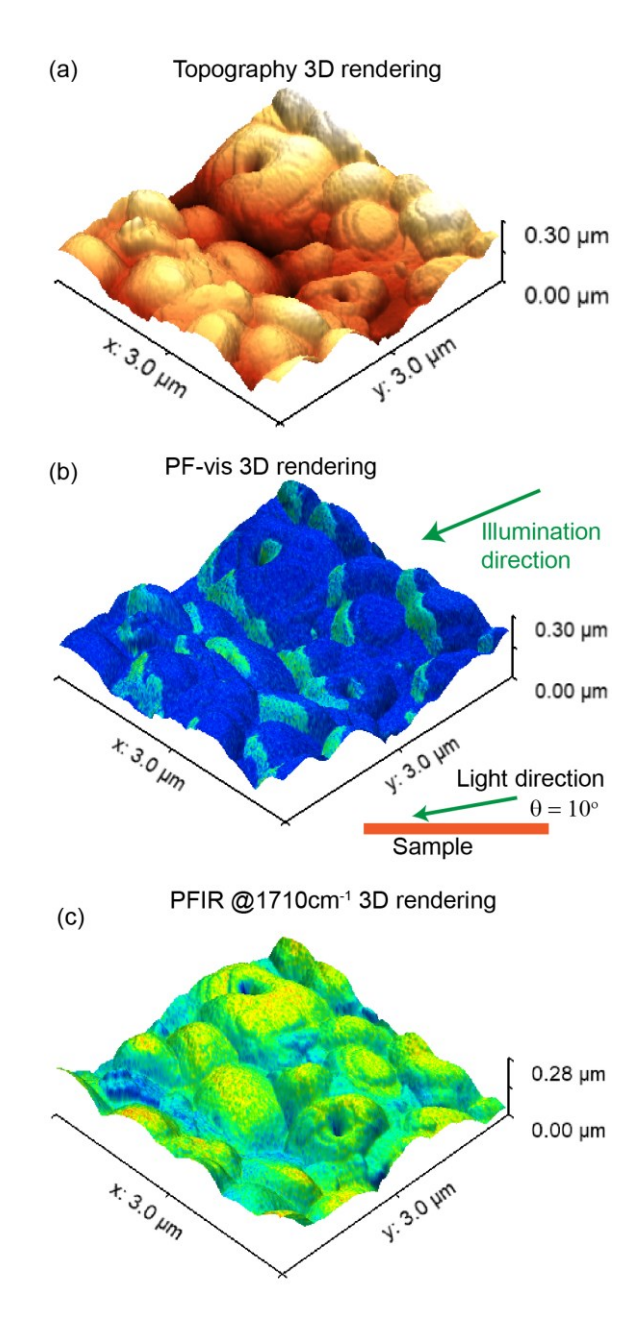


**Figure 4.** (a) 3D rendering plot of topography of the sample area. (b) 3D rendering plot of PF-visible signal overlaying on the topography. The data were collected simultaneously with data shown in Figure 2d. (c) 3D rendering plot of PFIR signal at 1710 cm<sup>-1</sup> overlaying on the topography. A regular plot of the data is shown in Figure 2c. The signals of (b) and (c) were collected in separate AFM scan frames.

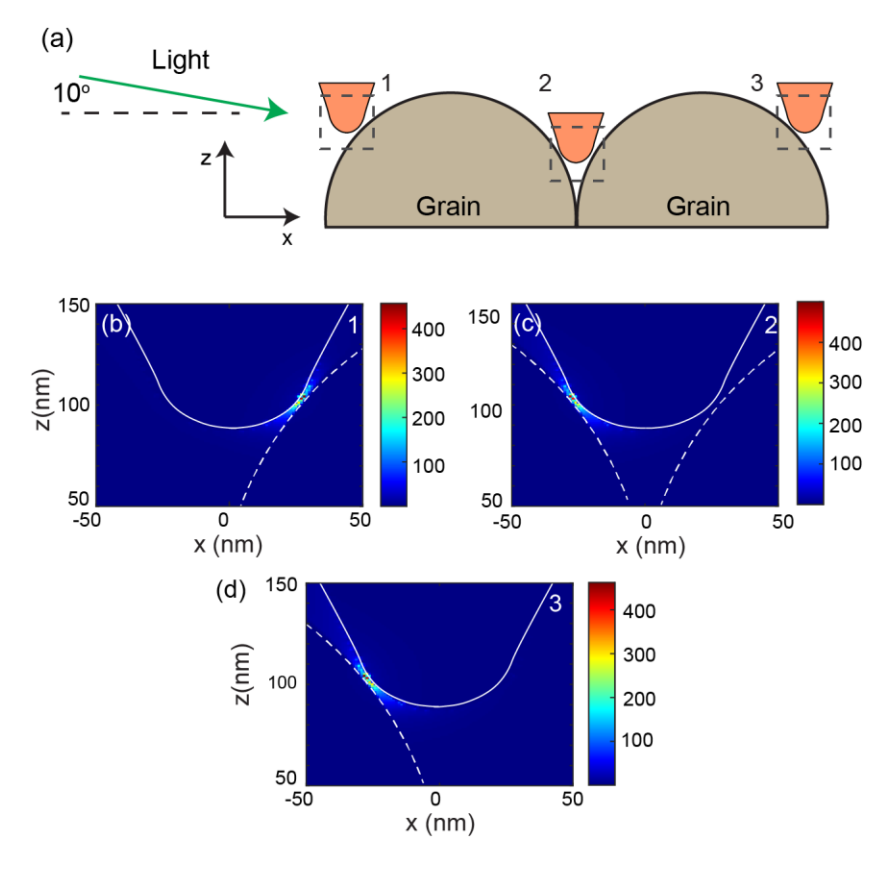


**Figure 5**. (a) The schematic configuration of the finite element simulation of perovskite grains and metallic AFM tips. The grazing angle of the light illumination is 10°. (b-d) The spatial distribution of the intensity of the electric field at regions marked by 1, 2, and 3 in (a). The gaps between the metallic AFM tip and the grains exhibit two orders of magnitude enhancement.

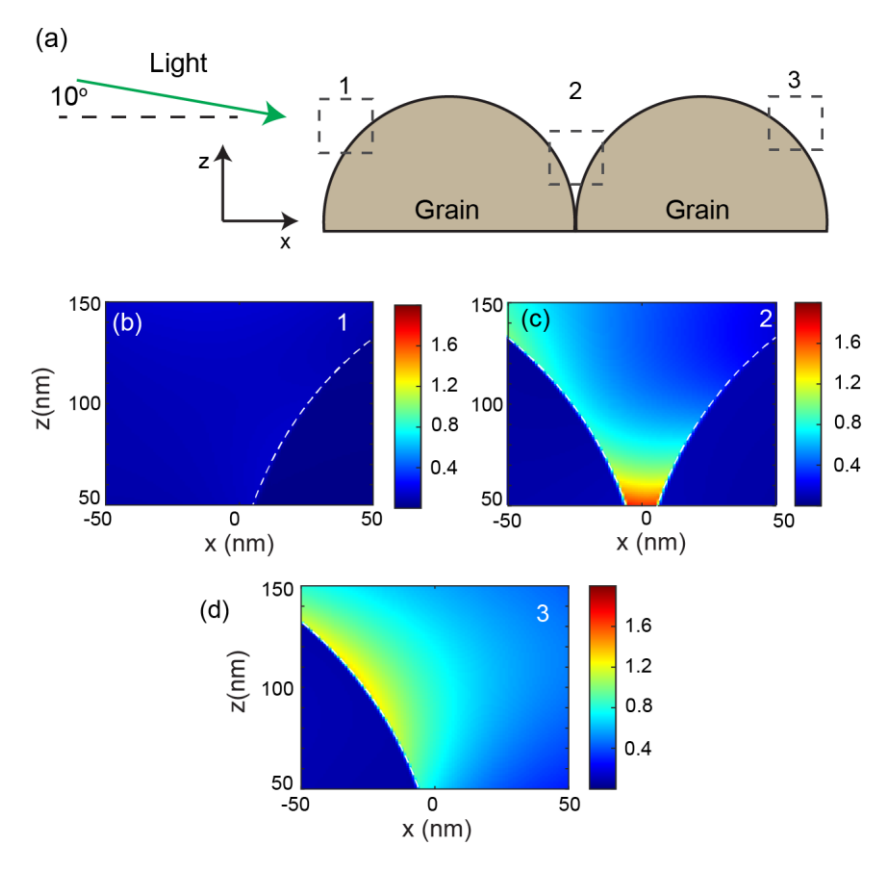


**Figure 6.** (a) The schematic configuration of the finite element simulation of perovskite grains only. The grazing angle of the light illumination is 10°. (b-d) The spatial distribution of the intensity of the electric field at regions marked by 1, 2, and 3 in (a). The back side of the grain exhibits stronger field than the front side of the grain.

